Solar Physics with Radio Observations, Proceedings of Nobeyama Symposium 1998, NRO Report 479

Radio and Hard X-Ray Observations of Flares and their Physical Interpretation

Markus Aschwanden[1]

[1] *Lockheed-Martin, Solar and Astrophys.Lab., Dept. H1-12, Bldg. 252, 3251 Hanover St., Palo Alto, CA 94304, USA*; *E-mail: aschwanden@sag.lmsal.com*

Abstract

We review a selection of observations in radio, hard X-rays (HXR) and soft X-rays (SXR) that constrain geometrical and physical requirements for solar flare models. Guided by observations of interacting flare loops we discuss a flare model based on shear-driven quadrupolar reconnection, which explains single-loop and double-loop flares in a unified picture. We interpret various observational findings in the light of this unified flare model:

- topology and geometry of interacting flare loops,
- localization of particle acceleration region,
- scale invariance of electron time-of-flight path and flare loop geometry,
- density and magnetic field diagnostic in acceleration region,
- bi-directionality of injected electron beams,
- electron beam trajectories and correlated HXR pulses,
- bifurcation of directly-precipitating and trap-precipitating electrons,
- density and magnetic field diagnostic of trap region,
- elementary time scales and dynamics in acceleration region.

Key words: Sun: flares — Sun: corona — Sun: radio — Sun: hard X-rays — Sun: soft X-rays

1. Introduction

Radio and hard X-ray (HXR) emission in solar flares complement each other ideally because both of them are produced largely by nonthermal electrons, but by different emission mechanisms. The underlying emission mechanisms are well-understood, i.e. plasma emission and gyro-synchrotron emission at radio wavelengths, and collisional bremsstrahlung in HXR, both requiring the interaction of nonthermal electrons with the density or magnetic field of the ambient plasma. Recent improvements in observational capabilities have achieved higher sensitivity and time resolution, which have been crucial for detailed timing analysis in radio and HXR. Systematic timing analysis on time scales of 10-100 ms allow us to relate the frequency-time drift rates (of radio bursts) and the energy-dependent time delays (of HXR pulses) to physical processes of adiabatic particle motion in flare loops. In this review we attempt to synthesize recent HXR and radio observations into a unified flare model.

2. Flare Models

2.1. Flare Loop Configuration

Many flare observations have been described in terms of a *single-loop* picture, with two magnetically conjugate footpoints seen in HXR, which are connected by a dipole-like loop that is bright in soft X-rays (SXR). While most of the HXR images show the omnipresent double footpoint sources (Duijveman, Hoyng & Machado 1982; Nitta, Dennis & Kiplinger 1990; Sakao 1994), only one single HXR source is detected occasionally ($\approx 30\%$; Sakao 1994). Such a single HXR source can be understood either as an unresolved double footpoint source, or as an incomplete detection of a strongly asymmetric footpoint pair, because the bipolar loop structure can often be traced to the undetectable footpoint with SXR images. Therefore, we can safely assume that a bipolar structure with two footpoints is the minimum magnetic configuration to explain a flare. An important detail that has been added to the *single-loop* picture is the occasional detection of a cusp-shaped structure above the flare loop, which can be seen in SXR (e.g.

Tsuneta et al. 1992; Forbes & Acton 1996), and coincides also with the location of coronal above-the-loop-top HXR sources discovered by Masuda et al. (1994).

However, recent analysis of HXR images from *Yohkoh/HXT*, SXR images from *Yohkoh/SXT*, and radio images from *Nobeyama* have revealed us additional spurs of the archetypal single-loop picture. Statistics of HXR footpoint sources show multiple (≥ 3) HXR sources in $\approx 30\%$ of the flares (Sakao 1994). In two recent studies with independent data sets (Hanaoka 1996; Nishio et al. 1997) it has been demonstrated that often a secondary large-scale ($\approx 30" - 80"$) loop is apparent in SXR and/or microwaves, besides the primary small-scale ($\approx 20"$) loop seen in SXR and HXR (see example in Fig.2c). The small-scale loop is always located near one footpoint of the large-scale loop, rendering the appearance of a *"three-legged"* structure. The latter observations have provided clear evidence for *interacting double loops*, a picture that has been anticipated already from observations with poorer spatial resolution (Machado et al. 1988).

2.2. Discussion of Flare Models

Like the observations, we can divide theoretical flare models into *single-loop* and *double-loop (or interacting loop)* models. However, the distinction between single and multiple loops cannot be sharply defined, because a single loop consists of a bundle of magnetic field lines, which can also be spread out along a neutral line, called an arcade. Depending on the spatial resolution, an arcade appears as a single loop or as a sequence of multiple loops. A physically more sensible distinction is perhaps to classify flare models according to their *bipolar* or *quadrupolar* magnetic topology. An arcade falls then into the category of *bipolar* structures and can be interpreted by the same flare models as a single loop.

Bipolar Flare Models: Sturrock (1966) proposed that a flare is created by shearing a bipolar arcade along a neutral line, which becomes then shear-unstable and undergoes magnetic reconnection at the Y-point, and can trigger a coronal mass ejection. Kopp & Pneuman (1976) and Hirayama (1974) used the same *helmet-streamer* topology for application of Y-type or X-type magnetic reconnection, which is driven by the dynamics of an upward erupting prominence and sideward compression at the X-point. Shibata et al. (1995) corroborated this model with Yohkoh observations of hot-plasma ejecta above flare loops. Tsuneta (1996) elaborated these models further by exploring shock formation in the outflow from the Petschek X-type reconnection point, at the downward interface to the SXR-bright flare loop. The fast shocks in the reconnection outflow were also related to Masuda's coronal HXR sources (Tsuneta et al. 1997). All these developments of bipolar flare models represent variants of X-type reconnection processes between two open (anti-parallel) magnetic field lines, and thus provide a natural explanation of cusp phenomena observed above flare loops. What is less clear, is the driver of X-type reconnection in these scenarios. Tsuneta (1996) invokes a lateral inflow of plasma at the X-point, which has not been detected with Yohkoh so far.

Quadrupolar Flare Models: The interaction between two closed magnetic field lines involves generally a quadrupolar magnetic topology, except for loops with parallel magnetic fields. Such loops with parallel magnetic fields are stable in a relaxed dipole field, and can interact only in the presence of currents, e.g. by anti-parallel currents (Gold & Hoyle 1960) or by coalescence of parallel currents (Sakai & Ohsawa 1987). A more likely possibility is the interaction of loops that stand in some angle to each other, configuring a quadrupolar magnetic topology. X-type reconnection by current loop coalescence between current-carrying flare loops with various orientations has been reviewed by Sakai & DeJager (1996). A crucial question is how the interacting loops are brought into contact before reconnection. Heyvaerts, Priest & Rust (1977) developed a model where a small-scale loop is emerging and reconnects with a pre-existing overarching large-scale flare loop. This model was favored by Hanaoka (1996) and Nishio et al. (1997) to explain their interacting, non-equal-sized flare loops. Quadrupolar reconnection was also employed by Somov, Kosugi, & Sakao (1997) and Longcope (1996). As an alternative to the emerging flux model of Heyvaerts et al. (1977), photospheric shear motion can be considered as a natural driver of quadrupolar reconnection (Aschwanden 1999). We describe this model in the next Section and will use it as a working hypothesis to interpret HXR and radio observations in the remainder of this review.

2.3. Flare Model of Shear-Driven Quadrupolar Reconnection

In the model of Heyvaerts et al. (1977), a new fluxtube emerges and reconnects with the overlying field. The emerging fluxtube is required to have a polarity oppositely-directed to the overlying field (in the 2D model of Heyvaerts et al.), in order to enable quadrupolar reconnection. The magnetic configuration of this 2D model involves therefore three neutral lines, one inside the emerging dipole, and two with respect to the pre-existing overlying dipolar field. However, this model is not consistent with the observations of Hanaoka (1996) and Nishio et al. (1997) for

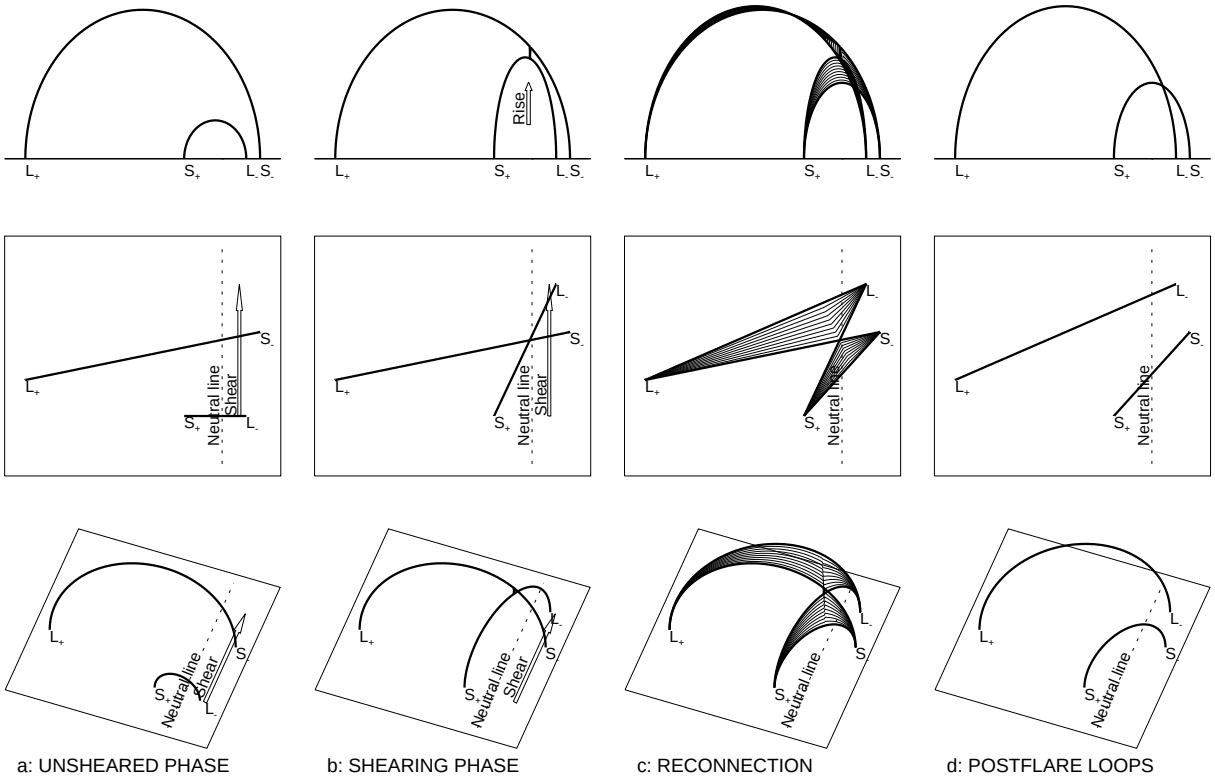

Fig. 1.. Side view (top row), top view (middle row), and perspective view (bottom row) of a shear-driven quadrupolar (3D) reconnection process. A small-scale loop becomes sheared (a) and comes into contact with an unsheared large-scale loop as consequence of the increasing footpoint separation (b), leading to X-point reconnection (c), with the endresult of two postflare loops that have exchanged connectivities, i.e. L_+, L_- for large-scale loop and S_+, S_- for small-scale loop (d). The appearance of a cusp (c) is a transient phenomenon during the relaxation of new-configured field lines. (Aschwanden 1999)

the following reason: The observations show generally a "three-legged" structure, i.e. the two interacting flare loops have one pair of footpoints close together with the same magnetic polarity, and thus cannot be reconciled (in any 2D projection) with the configuration of overlying oppositely-directed polarities as required by Heyvaerts et al. (1977). The "three-legged" structure involves only one neutral line, in contrast to the three neutral lines postulated in the model of Heyvaerts et al. (1997). Futhermore, the 2D model of Heyvaerts et al. (1977) cannot account for the observed angle between interacting flare loops (for example see Fig.2c). We consider now a 3D model with a *sheared quadrupole configuration*, which involves only one neutral line and appears to be more consistent with the magnetic topology of "three-legged" flare loop pairs as observed by Hanaoka (1996) and Nishio et al. (1997).

Shear motion along a neutral line has been recognized as an important condition for flaring. Flare locations have often been identified at particularly high-sheared segments of the neutral line (Hagyard et al. 1984; Hagyard, Venkatakrishnan & Smith 1990). Numerical simulations of sheared arcades have also demonstrated that sufficient non-potential magnetic energy can be built up to supply flares (Klimchuk & Sturrock 1992). A scenario of the *shear-driven quadrupolar reconnection model (SQR)* is depicted in Fig.1. The initial magnetic configuration is a set of field lines that cross a neutral line of an asymmetric dipole-like magnetic field. We characterize shearing within a shear zone that extends over a distance x_s from the neutral line and has a mean velocity v_s parallel to the neutral line. Loops that have their footpoint in this shear zone (with radius $r_0 < x_s$) become then sheared by an angle $\vartheta(t)$ that increases with time t as

$$\vartheta(t) = \arctan[\frac{v_s t}{2r_0}] \ , \tag{1}$$

stretching their footpoints apart with increasing separation. The response of the coronal loop segment to this increased footpoint separation is the relaxation to a dipole field, causing the apex of the stretched field line steadily to inflate. In the semi-circular approximation, the loop height or loop radius $r'(t)$ of the sheared small-scale loop

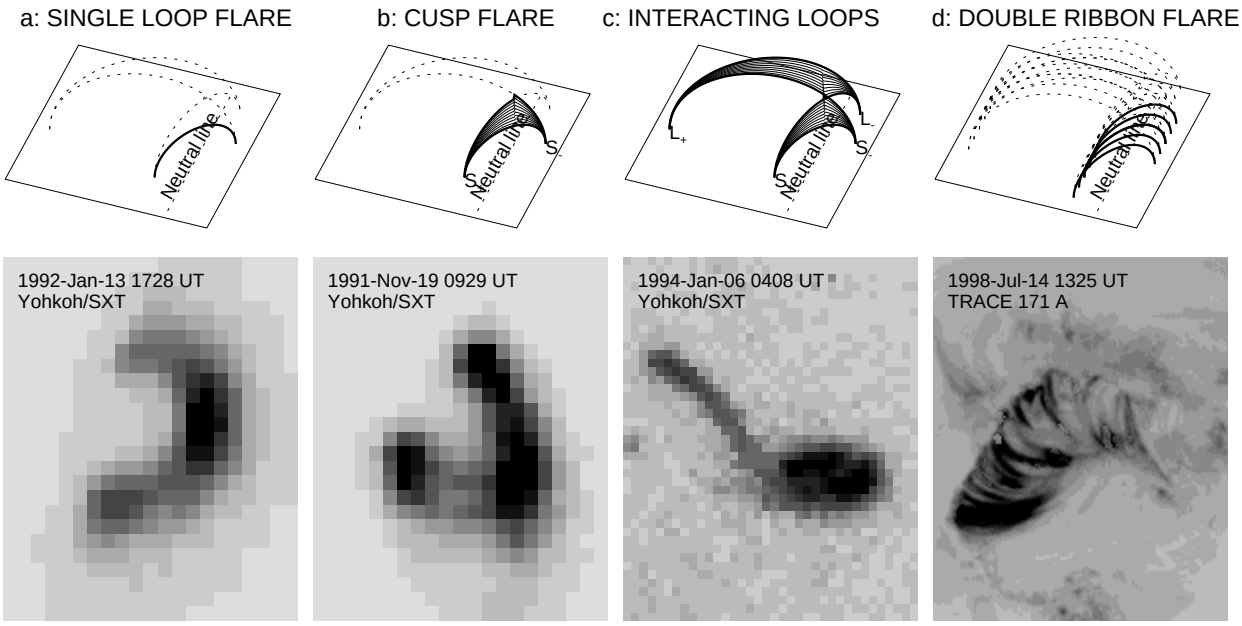

Fig. 2.. Four different manifestations of flare geometries produced by the shear-driven quadrupolar reconnection model (Fig.1). A *single-loop flare* (a) occurs if the secondary flare loop is not detected. For flares with long relaxation times, the cusp may be filled by chromospheric evaporation before the newly-reconnected field line is fully relaxed (b). *Interacting flare loops* (c) are visible if both reconnected field lines are filled by chromospheric evaporation. A *double ribbon flare* or an arcade of flare loops occurs if quadrupolar reconnection proceeds along the neutral line (d). An observational example is shown for each type of flares (bottom row), observed by *Yohkoh/SXT* (left 3 examples) or *TRACE* (right bottom).

increases as function of time t as

$$r'(t) = r_0 \sqrt{1 + \tan[\vartheta(t)]^2} \ . \tag{2}$$

A consequence of the footpoint shear motion is that the magnetic field between the top of the sheared small-scale loop and the overlying unsheared large-scale field (rooted outside the shear zone) becomes increasingly sheared and compressed. At some point the rising sheared loop will intersect with the unsheared large-scale loop and trigger a quadrupolar X-type reconnection. During quadrupolar reconnection, the connectivity of the field lines switches by exchanging the polarities of equal signs, producing two cusps between the two new-configured field lines. A natural consequence of this reconfiguration (of a highly-sheared small field line with a less-sheared large-scale field line) is that the new-configured small-scale field line has reduced shear, and thus ends up to be more stable than before reconnection. The new-configured cusp-like field lines slip then back from the X-point and relax into two dipole-like field lines, releasing magnetic energy during the shrinkage process by reducing the curvature of the magnetic field. The magnetic field change induces electric fields and wave turbulence, providing free energy to accelerate particles and heat the flare plasma. Most of the magnetic energy is released in the smaller cusp, because the change in the curvature of the magnetic field is strongest there. From this we expect that the reconfigured small-scale field line becomes the primary flare loop, where HXR bremsstrahlung and gyro-synchrotron emission from accelerated nonthermal electrons is more dominant than in the (new-configured large-scale) secondary flare loop. Note that this scenario explains also single-loop flares with a cusp, if the secondary large-scale flare is not detected.

2.4. Observed Flare Geometries

The *shear-driven quadrupolar reconnection model (SQR)* predicts a variety of flare topologies, depending on what fraction of the reconnected magnetic field lines become filled with heated plasma, e.g. by the chromospheric evaporation process. The most frequent appearance seems to be a *single loop* configuration with two conjugate HXR footpoints connected by a dipole-like SXR loop (Fig.2a). In the framework of the SQR model we expect such a single loop if most of the energy is released in the smaller cusp, and if the relaxation of the newly-configured field lines into a dipolar shape occurs faster or comparable with the filling delay of the heated plasma, which is typically ≈ 30 s for upflows in the chromospheric evaporation scenario (Mariska, Emslie, & Li 1989). In some flares where the relaxation of new-configured field lines, which have initially a cusp-shaped geometry, is slow, the upflowing plasma

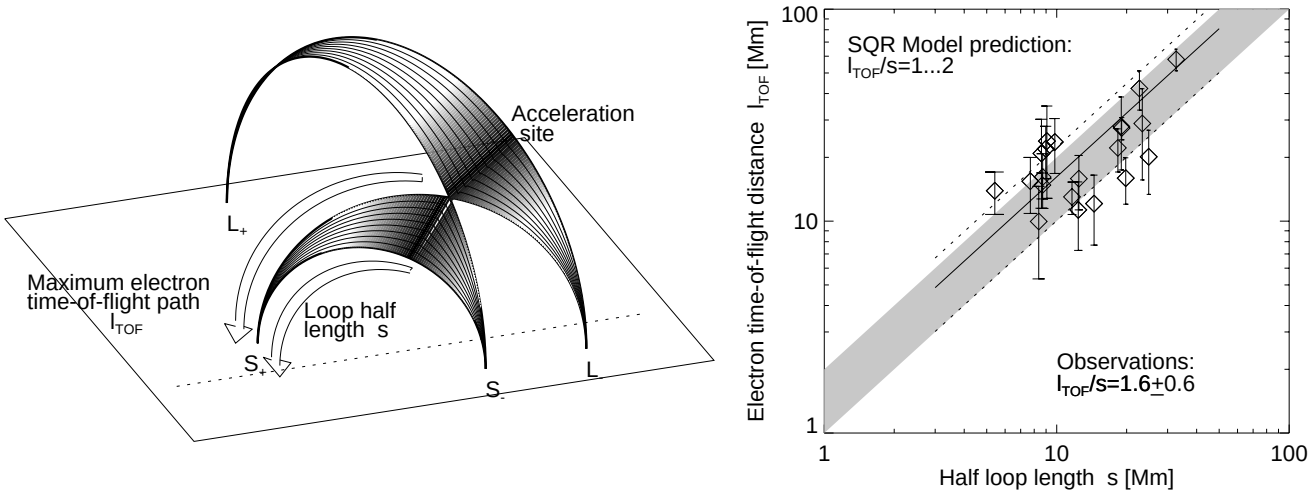

Fig. 3.. Predicted and observed scaling ratio between maximum electron time-of-flight path l_{TOF} and the loop half length s. The theoretical ratio is obtained from the length of the cusp segment to the relaxed dipolar segment in the primary flare loop, predicting a range of $l_{TOF}/s = 1...2$ (grey range in right-side panel). The observed ratio was found to be $l_{TOF}/s = 1.6 \pm 0.6$ (Aschwanden et al. 1996a; 1999).

may fill up the cusp-shaped field lines before they are relaxed into a dipolar shape (Fig.2b). This may apply to long-duration flares, e.g. as observed by Tsuneta et al. (1992) or Forbes & Acton (1996).

The classical case of the SQR scenario is the appearance of a pair of flare loops (Fig.2c), consisting of a small-scale loop with pronounced HXR footpoints, and a large-scale flare loop, both being visible in SXR and microwaves, as observed by Hanaoka (1996) and Nishio et al. (1997). Because these flare loops appear only bright in SXR after they become filled with heated plasma, we expect a delay of about ≈ 30 s for the small-scale loop in the chromospheric evaporation scenario, and an even larger delay for the large-scale loop [e.g. about 3 minutes for the 1994-Jan-06 0405 flare shown in Fig.2c]. During this time, both reconnected loops are likely to have relaxed into dipolar geometry. Thus, we expect to see two dipolar and disconnected postflare loops (Fig.2c).

While we considered only two field lines for quadrupolar reconnection so far, which may provide a sufficiently good approximation for highly localized flares, it is likely that the very same process can spread like an avalanche along an arcade of sheared field lines, if they reach a similarly critical state prone to quadrupolar reconnection. In this case we expect that small-scale flare loops are fired sequentially along a neutral line, forming an arcade with footpoints anchored along two parallel ribbons, as it has been observed in Hα wavelengths long ago and was dubbed *two-ribbon flares*. For an example of such a configuration we show a recent observation of *TRACE* in the EUV wavelength of 171 Å (Fig.2d), which shows an arcade of postflare loops, sequentially cooling down to a temperature of ≈ 1 MK. The image shown in Fig.2 (right) is taken 20 minutes after the impulsive phase. This arcade consists of about 20 resolved postflare loops, each one sheared by about 45^0 to the neutral line. The equivalent case of such a two-ribbon flare in radio wavelengths, which visualizes the gyrosynchrotron emission of trapped high-energy electrons in the magnetic mirror field above the neutral line, is shown in the review by Bastian (1999) in this Proc.

3. Particle Kinematics

3.1. Particle Acceleration Region

The site of energy release and concomitant particle acceleration in our *shear-driven quadrupolar reconnection model* is likely to be associated with the changes of the magnetic field in the cusp region where the new-configured magnetic field lines relax from an initial cusp shape to a dipolar geometry. The reconnected magnetic field lines shorten during the relaxation process, and thus provide free energy due to the shortening of the field line (dB/ds) and due to the change in field curvature (dB/dr). The change of the magnetic field (dB/dt) induces an electric field $\mathbf{E}$ according to the Maxwell equation

$$\nabla \times \mathbf{E} = -\frac{1}{c}\frac{d\mathbf{B}}{dt} \ , \tag{3}$$

similarly to the acceleration process in a betatron. While the detailed mechanism of particle acceleration in the time-varying magnetic fields and the related stochastic acceleration via wave turbulence in the envisioned quadrupolar reconnection geometry needs to be worked out in future theoretical studies, we can say at least that the site of particle acceleration is most likely to be located where the magnetic field (dB/dt) changes most rapidly, i.e. near the cusp region, during the initial "slip-back" phase after reconnection, while the acceleration efficiency will asymptotically slow down when approaching the relaxed dipolar field.

The probably most constraining information on the localization of the particle acceleration site comes from electron time-of-flight measurements, which quantify the distance between the acceleration site and the chromospheric flare loop footpoints, where the energy-dependent timing of thick-target HXR bremsstrahlung can be used to infer the electron propagation path length l_{TOF}. This distance was found to scale with the primary flare loop half length s (Fig.3 right) with a scale-invariant ratio of $l_{TOF}/s = 1.6 \pm 0.6$ (Aschwanden et al. 1996a; 1999). The maximum electron time-of-flight distance can directly be calculated in our SQR model. A typical value can be obtained by assuming a high shear angle ($\vartheta \lesssim 90^0$) and reconnection near the apex of the small-scale loop. For this simplified geometry, the scaling ratio of the maximum electron time-of-flight distance (defined by the half length of the cusp-shaped small-scale loop before reconnection) to the half length s of the relaxed small-scale postflare loop can be expressed as (Aschwanden 1999)

$$\frac{l_{TOF}}{s} = 2\sqrt{\frac{A}{(1+A)}} \ , \tag{4}$$

where A denotes the asymmetry ratio of the footpoint distances of the unsheared large-scale loop to the neutral line. Thus the scaling ratio varies from $l_{TOF,max}/s = \sqrt{2} = 1.4$ for symmetric loops ($A = 1$) to $l_{TOF,max}/s = 2$ for strongly asymmetric loops ($A \gg 1$). These ratios are inferred from the length of the cusp field line segment, which represents an upper limit for the maximum electron time-of-flight distance. If we assume that particle acceleration is feasible in the entire cusp area, the ratio could be as low as ≈ 1. Thus, from the SQR model we predict a range of $l_{TOF} = 1...2$, which is fairly consistent with the range of observed values, $l_{TOF}/s = 1.6 \pm 0.6$ (Aschwanden et al. 1996a; 1999).

The previous discussion considered only the average timing of HXR emission from the two conjugate footpoints of the primary flare loop. If HXR emission is seen from a third footpoint, most likely from the closer footpoint of the secondary (large-scale) flare loop, the timing will be almost identical to that from the footpoints of the primary flare loops because of the similar geometric length of the involved loop segment. The scaling law l_{TOF}/s will therefore not be modified. Only if HXR emission from a forth HXR source is seen, supposedly from the remote footpoint of the large-scale (secondary) flare loop, the timing will be substantially delayed. Hanaoka (this Proc.) analyzed the timing of such a remote HXR source and found it to be consistent with an ≈ 4 times longer time-of-flight distance. Such a contribution would of course increase the "averaged" scaling law l_{TOF}/s by a factor weighted by the relative flux contribution.

3.2. Bi-Directional Electron Beams

The frequency-time drift rate $d\nu/dt$ of radio bursts provides a measurement of the propagation velocity and direction of electron beams emanating from the acceleration site. Upward propagating electron beams can be detected along open field lines and closed field lines (metric type III, J, and U bursts), while downward propagating electron beams are detectable in form of *reverse-slope (RS)*-drifting bursts. Our shear-driven quadrupolar reconnection model involves two closed field lines, which reconfigure into two cusp-shaped field lines after reconnection. While these two cusp-shaped field lines relax into a dipolar geometry, the electric fields induced by the change of the magnetic field (Eq.3) and the associated wave turbulence provides free energy to accelerate particles, which can escape from the cusp region in all four directions of the reconfigured field lines. One direction leads initially upwards, along the (secondary) large-scale loop, where we expect to see type J and U bursts, while all other three directions lead downwards, where we might see some RS bursts. In summary, the model predicts bi-directional electron beams in upward and downward direction due to the geometric symmetry of the acceleration site at the X-type reconnection point (Fig.4), in particular pairs of type U-bursts and RS-bursts for each elementary reconnection episode. However, the efficiency of producing plasma emission depends on several factors that makes the probability for detection quite different in upward and downward direction. Upward-accelerated electrons encounter a decreasing magnetic field, which has a focusing effect on the pitch-angle distribution of a beam and makes it more prone to plasma emission. Also, the lower density encountered in upward direction makes it easier for plasma emission to escape. These two properties may be the main reason why upward propagating electrons are detected much more frequently (in form

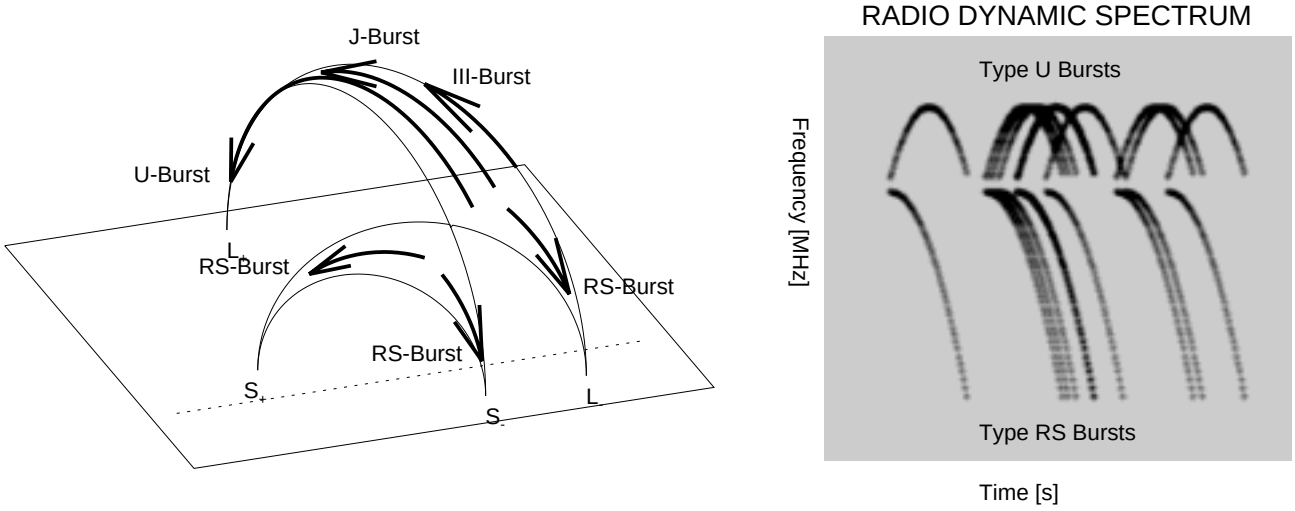

Fig. 4.. Spatial trajectories of radio bursts in the shear-driven quadrupolar reconnection model (left frame) and corresponding representation in a radio dynamic spectrum (right frame). A quasi-periodic sequence of acceleration episodes produces synchronized electron beams in upward (type III, J, and U-bursts) and downward direction (reverse-slope [RS] bursts).

of type III, J, and U bursts) then downward propagating electron beams (RS bursts). Our SQR model predicts also that upward accelerated electron beams move along closed field lines, and thus return to the lower corona at the remote opposite footpoint without having access to interplanetary space. This scenario explains therefore in a natural way the overabundance of downward accelerated electrons (as calculated from HXR spectra) compared with the number of electrons escaping into interplanetary space (as detected in situ). The number of electrons (above ≈ 20 keV) escaping into the interplanetary medium was estimated from 0.6% (Holt & Ramaty 1969) down to 0.1% (Lin 1974). Type III bursts that escape towards higher solar altitudes and into interplanetary space can only be produced in our model if an open field line is involved in the reconnection process in first place, or if some large-scale field lines disconnect in a secondary step and open up.

3.3. Correlated Radio Bursts and HXR Pulses

The temporal coincidence between radio bursts and HXR pulses, which are produced by thick-target bremsstrahlung of electron beams precipitating down to the chromosphere, establishes the reality of bi-directional electron acceleration additionally. An example of a combined radio and HXR flare observation is reproduced in Fig.5 (from Aschwanden et al. 1995a). The >28 keV HXR flux shows a sequence of about 9 pulses with a mean time interval of $P = 2.2$ s. Each HXR pulse is correlated with a metric type U-burst, which are delayed by $t_R - t_X = 0.61$ s in the average. The center frequency of the metric type U-bursts is $\nu \approx 250 - 300$ MHz, corresponding to an electron density of $n_e \approx 0.8 - 1.1 \cdot 10^9$ cm^{-3}. This observation, which is typical for many flares, is fully consistent with the SQR model, where subsequent reconnection events modulate synchronized acceleration in upward and downward direction. The expected observational signatures are: (1) a quasi-periodic sequence of type U bursts with similar turnover frequencies produced by upward propagating electron beams, (2) correlated HXR pulses produced in the chromosphere by bremsstrahlung of downward precipitating electron beams, (3) the electron density in the secondary flare loop (where type U-bursts are produced) is lower ($n_e \approx 10^9$ cm^{-3}) than in the SXR-bright primary flare loop (with typical densities of $n_e \approx 10^{11}$ cm^{-3}), (4) upward propagating electron beams are delayed with respect to the HXR pulses, because of their longer propagation time and lower velocity. Examples of type U-bursts that clearly demonstrate that the secondary large-scale flare loop has generally a much larger dimension (with heights of $h \approx 100,000...200,000$ km) than the primary flare loop (with typical heights of $h = 3000...20,000$ km) are documented in studies with imaging observations (e.g. Aschwanden et al. 1992; Pick et al. 1994; Aurass & Klein 1997).

Sometimes, both the upward and downward propagating electron beams are detected in radio. Examples of such bi-directional electron beams are shown in Fig.6. From the relative time delay of the downward propagating electron beams detected in HXR and radio, which amounted to $t_R - t_X = 0.27 \pm 0.15$ s in a well-analyzed flare (Aschwanden, Benz, & Schwartz 1993), it was concluded that the radio-emitting electrons have a lower energy ($\lesssim 5$ keV) than

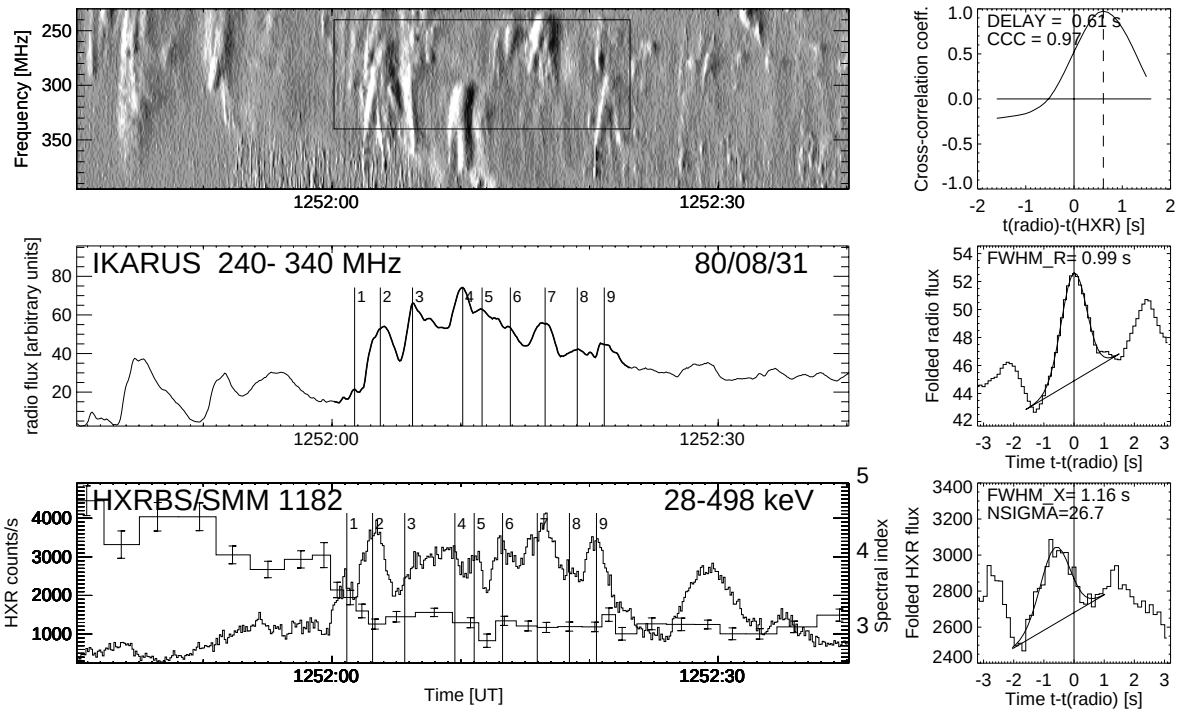

Fig. 5.. Radio dynamic spectra (from spectrometer PHOENIX of ETH Zurich) and HXR data (from *Hard X-Ray Burst Spectrometer (HXRBS)* onboard the *Solar Maximum Satellite (SMM)* of the flare 1980-Aug-31, 1252 UT. The radio data show mainly type U-bursts in coincidence with 9 HXR pulses. According to cross-correlation of all superimposed 9 time profiles, the radio bursts are delayed by $t_R - t_X = 0.61$ s (right top). The evolution of the spectral index is shown in histogram representation with error bars (bottom panel, right axis). [from Aschwanden et al. 1995a].

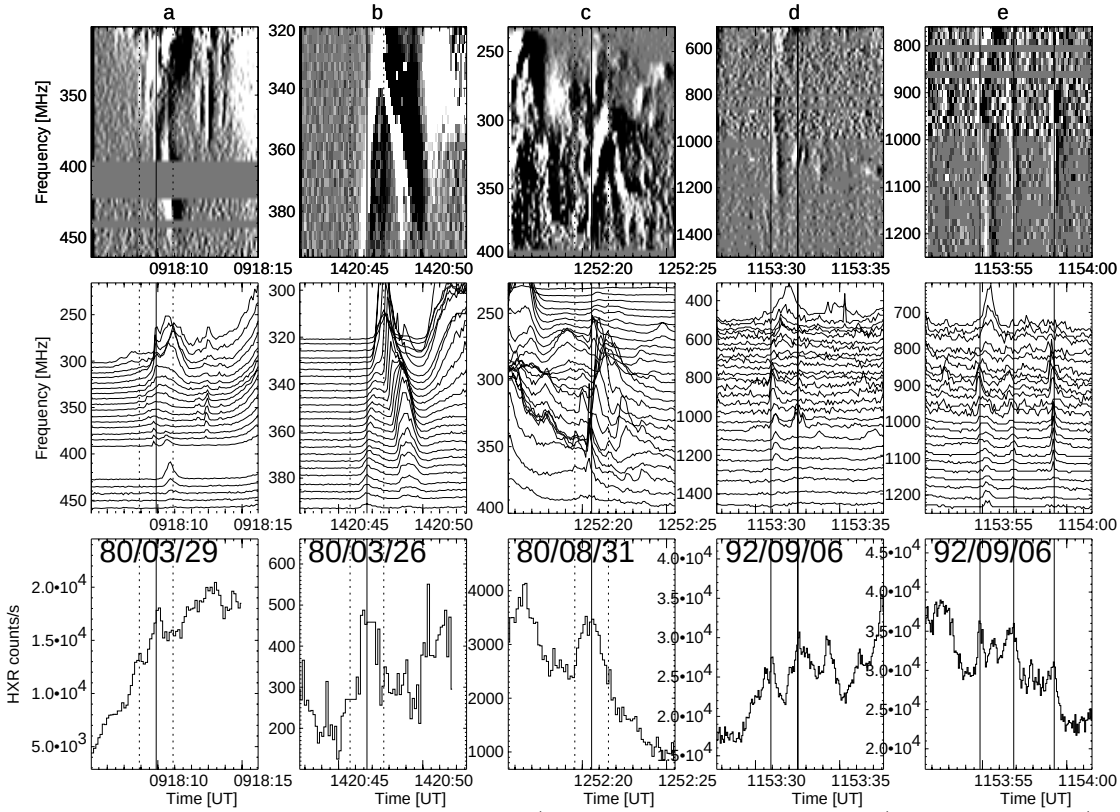

Fig. 6.. Detailed correlations between individual radio bursts (top and middle row; ETH Zurich) and HXR pulses (bottom row; HXRBS/SMM and BATSE/CGRO): (a,d,e) oppositely-drifting burst pairs, consisting of type III and RS bursts, and (b,c) type U-bursts. Each time interval is 10 s. (From Aschwanden et al. 1995b).

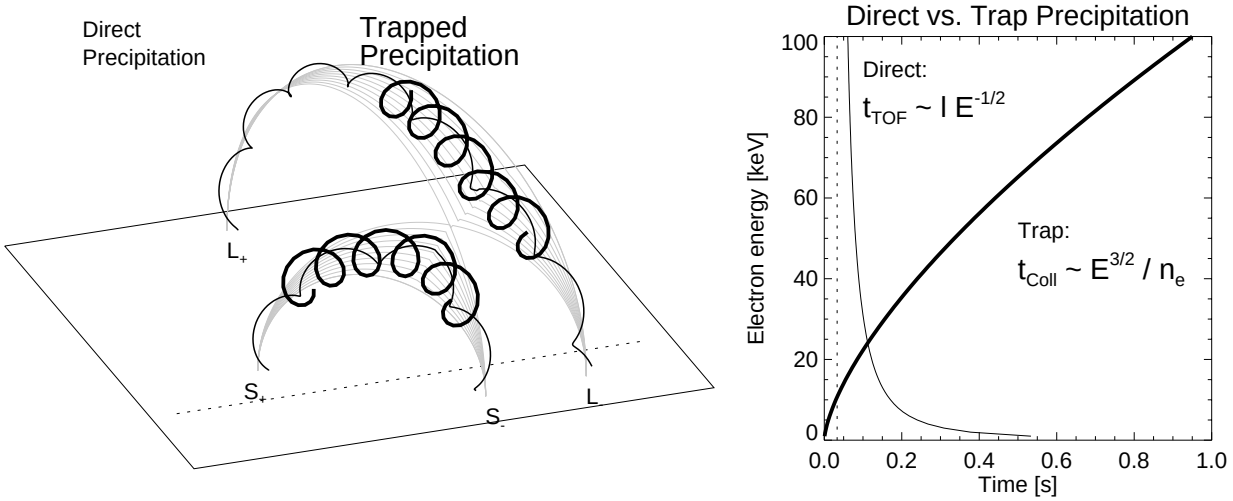

Fig. 7.. Bifurcation of electron trajectories as function of the initial pitch angle (left). Electrons with small initial pitch angle precipitate directly and their timing is given by the time-of-flight interval $t_{TOF} = l/v \approx l * E^{-1/2}$. Electrons with large initial pitch angles are intermediately trapped, until they become scattered into the loss-cone, latest after a collisional deflection time, $t_{Coll} \propto E^{3/2}/n_e$. The energy-dependent timing for the two processes is compared for a propagation distance of $l = 10^9$ cm and an electron density of $n_e = 10^{11}$ cm^{-3} (right-hand panel).

the HXR-emitting electrons ($\gtrsim 25$ keV). It is not clear whether this lower energy applies generally to coronal radio bursts (although fast-drift radio bursts are generally found to be delayed by a few 100 ms with respect to a correlated HXR pulse), because little imaging information is available to pinpoint the trajectories of radio-emitting electrons with sufficient accuracy.

3.4. Electron Density Diagnostics

The start frequency of radio bursts that produce plasma emission provides a useful electron density diagnostic of the acceleration site. A systematic search of bi-directional electron beams in radio dynamic spectra, by detecting a simultaneous start of an upward propagating electron beam (type III burst) and a downward propagating electron beam (type RS burst), revealed a range of electron densities $n_e = 10^9 - 10^{10}$ cm^{-3} for the acceleration site in 30 flares (Aschwanden et al. 1995b).

Using the SXR emission measure EM measured in resolved flare loops with loop diameters d to determine the electron density $n_e \approx \sqrt{EM/d}$ of the heated flare plasma, Aschwanden & Benz (1997) find a mean density of $n_e^{SXR} = (0.2 - 2.5)\ 10^{11}$ cm^{-1} in these SXR loops, while the simultaneously measured electron densities from start frequencies of type III bursts yield a much lower value, $n_e^{radio} = (0.6 - 10)\ 10^9$ cm^{-3}. The average density ratio is found to be $n_e^{radio}/n_e^{SXR} = 0.005 - 0.13$. This result implies that the electron density is 1-2 orders of magnitude lower in the acceleration site than in the flare loop that contains the heated flare plasma. This result clearly rules out that the acceleration site is located inside the SXR flare loop. The radio-inferred electron density values place therefore the acceleration site in a low-density region (being 1-2 orders of magnitude lower than the SXR loop), which must be substantially displaced above the apex of the SXR flare loop. In our SQR model we expect a much lower electron density in the acceleration region as long as the cusp is not filled up by heated plasma through the chromospheric evaporation process. However, after a filling delay of ≈ 30 s we expect that the upflowing plasma engulfs the apex of the relaxing new-reconnected field lines.

3.5. Direct-Precipitation versus Trap-Precipitation

Timing analysis of HXR has shown that there are at least two different processes that determine the energy-dependent timing. Subsecond pulses in HXR time profiles were found to be consistent with electron time-of-flight differences occurring over a distance of about 1-2 times the primary flare loop half length. The energy-dependence of these directly-precipitating electrons is

$$t_{TOF}(E) = \frac{l_{TOF}}{v} \approx l_{TOF}\ E^{-1/2} \tag{5}$$

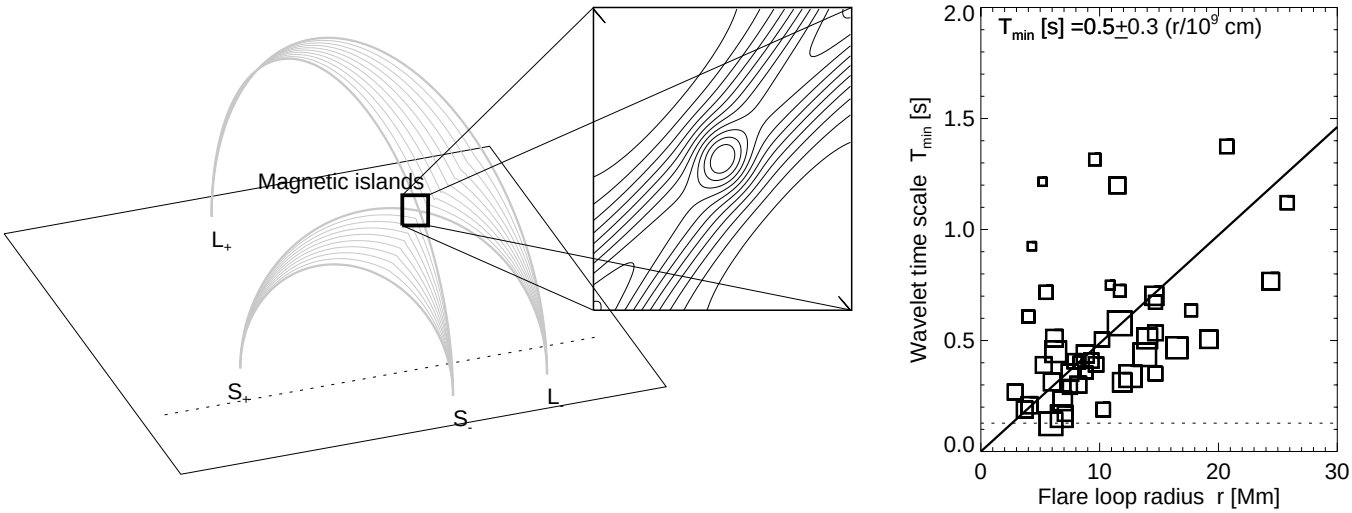

Fig. 8.. The theoretical model of shear-driven quadrupolar reconnection predicts formation of magnetic islands in the X-type reconnection point (left), which have been simulated numerically by Karpen et al. 1995 (see enlarged sketch in middle frame). The correlation found between wavelet time scales T_{min} and flare loop radius r (right frame, from Aschwanden et al. 1998b) is interpreted in terms of a scale-invariant ratio of magnetic islands sizes and flare loop sizes.

in the non-relativistic limit. These electrons are required to have small initial pitch angles, in order to reach the chromospheric footpoints through the possibly converging magnetic field.

On the other hand, the smoothly-varying HXR flux was found to obey an oppositely-directed energy-dependent timing, consistent with the collisional deflection time,

$$t_{Defl}(E) \approx 10^8 (\frac{E^{3/2}}{n_e}) \ [s] \ . \tag{6}$$

The propagation characteristics of those electrons that contribute to the smoothly-varying HXR flux was therefore attributed to intermediate trapping in the magnetic mirror field between the conjugate footpoints (Aschwanden et al. 1996b; 1997, 1998a). In our SQR model, thie mirror field is naturally explained by the converging field that characterizes the cusp region above the flare loops (Fig.7, left). Such a cusp-shaped magnetic mirror field was also employed to explain the above-the-loop-top HXR emission discovered by Masuda et al. (1994), by using numerical Fokker-Planck simulations to mimic trapping in the surroundings of the acceleration region (Fletcher & Martens 1997). Electron trapping is not only necessary to explain the delays of the smoothly-varying HXR component, but also the delays of gyrosynchrotron emission with respect to HXRs (Bastian, Benz, & Gary 1998). It turns out that the gyrosynchrotron-emitting electrons display a time delay not only with respect to direct-precipitating electrons manifested in the prompt HXR pulses, but also with respect to the trap-precipitating HXR component, probably because of the longer trapping times expected for higher energies (Bastian 1999). However, although the collisional deflection time is found to match well the HXR delays for energies of 25-200 keV, it is expected that trapping times at higher energies are shorter due to wave turbulence (*strong-diffusion regime*; e.g. Ramaty et al. 1994). The location and polarization of radio sources in flares analyzed by Hanaoka (1996) and Nishio et al. (1997) are consistent with the geometry of trap regions expected in our SQR model (Fig.7), often detected in both the primary and secondary flare loop, located near the footpoints for high microwave frequencies (or vice versa, i.e. closer to the loop tops for lower microwave frequencies).

3.6. Particle Dynamics in Acceleration Region

While the dynamics of propagating particles is fairly well-understood in solar flare loops, the dynamics of the acceleration process and the associated time structures are least understood. Propagation effects could been disentangled mainly from energy-dependent time delays, which have a characteristic energy dependence. However, it is still not clear whether the acceleration process produces also energy-dependent time delays and how it produces the elementary time structures that are observed in radio and HXRs.

A crucial problem in the analysis of time structures is the multi-scale behaviour that governs time series with fractal properties. A recent study with a wavelet analysis of some 700 HXR (>25 keV) time profiles (Aschwanden et al. 1998b) revealed an important new result on the spatio-temporal organization of flares. In strong flares, where

fast (sub-second) time structures clearly exceed the significance threshold of Poisson noise, the shortest time scales detected with a wavelet method were found in a range of $T_{min} = 100 - 700$ ms. These minimum time scales were found to correlate with the flare loop size r, as measured from the footpoint separation in *Yohkoh/SXT* and *HXT* images, according to the relation (Fig.8 right panel)

$$T_{min}(r) \approx (0.5 \pm 0.3)(\frac{r}{10^9\ cm})\ [s]\ . \tag{7}$$

The scatter of this correlation is partially attributed to the accuracy of the employed wavelet algorithm (within a factor of 2), to confusion by multi-scales, and to Poisson noise in the case of weak flares. Note, that the so-determined wavelet time scales are essentially energy-independent, because HXR subsecond pulses have no significant difference in their duration at different energies (Fig.4 in Aschwanden, Schwartz, & Alt 1995). Moreover, these minimum timescales were also found to be subject to a cutoff that corresponds approximately to the collisional deflection time,

$$T_{min}(E) \gtrsim t_{Defl}(E) \tag{8}$$

These results suggest that the fastest significant HXR time structures are related to physical parameters of propagation and collision processes in the acceleration region. If we associate the minimum time scale T_{min} with an Alfvénic crossing time through an elementary acceleration cell, we obtain sizes of $r_{acc} \approx 75 - 750$ km, which have a scale-invariant ratio of $r_{acc}/r \approx 3\%$ to flare loops and are also consistent with cell sizes inferred from the frequency bandwidth of decimetric millisecond spikes (Benz 1986). Because HXR emission is always dominated by the small-scale (primary) flare loop, the scaling law $T_{min}(r)$ given here applies to the smaller flare loop (with radius r).

What is the physical mechanism that generates these scale-invariant spatial structures in the acceleration region, which seem to be formed in a cyclic sequence or modulated by a quasi-oscillatory mechanism? At this point we can only speculate, until more physical parameters and scaling laws are established by observations. Magnetic island formation occurring during the shear-driven tearing mode instability represents a theoretical candidate. Oscillatory dynamics of coalescing current sheets has been studied earlier (e.g. Smith 1977; Spicer 1981, Sakai & Ohsawa 1987). Recent numerical simulations of reconnection-driven current filamentation show clearly the formation of magnetic islands (e.g. Karpen et al. 1998). The particle orbits in the neighbourhood of an X-type reconnection point or an O-type magnetic island are, besides the accelerating fields, also subject to secondary forces (such as ∇B drift or $E \times B$ drift), which have not been simulated in detail for the magnetic field geometry envisioned by our SQR model (but see Kliem 1994 for an example of such numerical simulations). Nevertheless we like to emphasize that the scaling laws inferred from the wavelet analysis, i.e. $T_{min}(r)$ and $T_{min}(E)$ (Eqs.7,8), may provide substantial constraints on the physical properties of magnetic island formation in the reconnection region.

4. Summary and Conclusions

The aim of is review is to synthesize recent flare observations in HXR, SXR and radio into a consistent big picture. As a starting point we reviewed various observed flare loop configurations, which provide important guidance to judge the applicability of theoretical flare models. In particular, they shed some light on the magnetic topology of flares: Can a flare be understood in terms of a single dipolar loop? Does the occasionally observed cusp geometry indicate a 2D-reconnection scenario? Or do interacting flare loops require a 3D-reconnection model with a quadrupolar configuration? As a working hypothesis we adopted a quadrupolar reconnection approach that is sufficiently general to explain single loop flares, cusp-shaped flares, interacting loop flares, or arcade-like double-ribbon flares. As a natural driver of quadrupolar reconnection we considered photospheric shear motion, which inflates small-scale loops near the neutral line and forces them to reconnect with unsheared overlying large-scale loops. This process my act in concert with the emergence of twisted flux tubes, but requires a less fragmented magnetic topology than the emerging-flux model of Heyvaerts et al. (1977).

We discussed the observational consequences of the shear-driven quadrupolar reconnection model. The X-type reconnection process produces cusp-shaped field lines which slip back into a relaxed dipolar configuration. This relaxed dipolar configuration with reduced shear is the expected outcome that is observed in the postflare phase. Because of the filling delay (of heated plasma by chromospheric evaporation) we probably can never observe the reconnection itself, but rather the relaxation phase thereafter. Nevertheless, the geometry of the relaxed postflare loops allows us to reconstruct the position of the X-type reconnection point and the geometric shrinkage ratio of the new-configured relaxing field lines. From simple geometric considerations we find a scaling ratio of $l_{TOF}/s = 1...2$ between the initial length of new-configured field line segments and the fully relaxed dipolar end state. If we associate the change of the magnetic field in the shrinking cusp with the free energy source for particle acceleration and heating,

we can explain the observed scaling ratio of electron time-of-flight paths, i.e. $l_{TOF}/s = 1.6 \pm 0.6$. Particle acceleration in the transiently cusp-shaped field lines are expected to produce bi-directional electron beams, manifested as upward (type III, J, U) and downward (type RS) directed radio bursts. The plasma frequency of the radio bursts allows for a convenient density diagnostic. Observations confirm that the density in the acceleration region is about 1-2 orders of magnitude lower than in the SXR-bright flare loops, which are filled with chromospheric plasma. Each acceleration episode is also expected to produce a correlated HXR pulse in the chromospheric footpoints, triggered by directly-precipitating electrons. Timing analysis of the energy-dependent HXR flux has shown that two pitch-angle domains can be distinguished: (1) electrons with small pitch angles precipitate within time-of-flight, while (2) electrons with large pitch angles seem to be intermediately trapped until they become scattered into the losscone by collisional deflection. Radio and HXR time profiles reveal often fast (sub-second) time structures that seem to be produced in the acceleration region. A wavelet analysis has demonstrated that these sub-second time scales are correlated with the flare loop size, having a scale-invariant ratio of $\approx 3\%$. In the physical model of shear-driven reconnection, it is likely that these intrinsic time scales are attributed to the spatial sizes of magnetic islands, which form as a result of the tearing-mode instability and modulate particle acceleration and injection. The magnetic mirror field in the cusp region governs also the gyrosynchrotron emission of trapped electrons. The timing and spectum of gyrosynchrotron emission is discussed in a recent review (Bastian, Benz, & Gary 1998) and by Bastian (1999) in this Proc.

Acknowledgements: The author would like to thank many colleagues and collaborators for useful comments and discussions. This work was supported by NASA contract NAS8-40108 (Yohkoh/SXT data analysis). The Yohkoh data used in this paper are taken by the Yohkoh mission of ISAS, Japan, which was prepared and is operated by the international collaboration of Japanese, US, and UK scientists under the support of ISAS, NASA, and SERC, respectively. We thank Dr. Alan Title for unpublished TRACE data. The TRACE team includes scientists from Lockheed Martin Advanced Technology Center, Stanford University, NASA Goddard Space Flight Center, the University of Chicago, Montana State University, and the Harvard-Smithsonian Center for Astrophysics.

References

Aschwanden,M.J. 1999, ApJ, in preparation
Aschwanden,M.J., Bastian,T.S., Benz,A.O., and Brosius,J.W. 1992, ApJ 391, 380
Aschwanden,M.J. and Benz,A.O. 1997, ApJ 480, 825
Aschwanden,M.J., Benz,A.O., Dennis,B.R., and Schwartz,R.A. 1995b, ApJ 455, 347
Aschwanden,M.J., Benz,A.O. and Schwartz,R.A. 1993, ApJ 417, 790
Aschwanden,M.J., Bynum,R.M., Kosugi,T., Hudson,H.S., and Schwartz,R.A. 1997, ApJ 487, 936
Aschwanden,M.J., Fletcher,L., Sakao,T., Kosugi,T., and Hudson,H. 1999, ApJ, in press
Aschwanden,M.J., Kliem,B., Schwarz,U., Kurths,J., Dennis,B.R., and Schwartz,R.A. 1998b, ApJ 505, 941
Aschwanden,M.J., Kosugi,T., Hudson,H.S., Wills,M.J., and Schwartz,R.A. 1996a, ApJ 470, 1198
Aschwanden,M.J., Montello,M.L., Dennis,B.R. and Benz,A.O. 1995a, ApJ 440, 394
Aschwanden,M.J., Schwartz,R.A., and Dennis,B.R. 1998a, ApJ 502, 468
Aschwanden,M.J., Schwartz,R.A., and Alt,D.M. 1995, ApJ 447, 923
Aschwanden,M.J., Wills,M.J., Hudson,H.S., Kosugi,T., and Schwartz,R.A. 1996b, ApJ 468, 398
Aurass,H., and Klein,K.L. 1997, AASS 123, 279
Bastian,T.S. 1999, in this Proc.
Bastian,T.S., Benz,A.O., and Gary,D.E. 1998, Annu.Rev.Astron.Astrophys. 36, 131
Benz,A.O. 1986, Solar Phys. 104, 99
Duijveman,A., Hoyng,P., and Machado,M.E. 1982, Solar Phys. 81, 137
Fletcher,L., and Martens,P.C.H. 1997, ApJ 505, 418
Forbes,T.G. and Acton,L.W. 1996, ApJ 459, 330
Gold,T. and Hoyle,F. 1960, MNRAS 120/2, 89
Hagyard,M., Smith,J.B.Jr., Teuber,D., and West,E.A. 1984, Solar Phys. 91, 115
Hagyard,M.J., Venkatakrishnan,P., and Smith,J.B.Jr. 1990, ApJS 73, 159
Hanaoka,Y. 1996, Solar Phys. 165, 275
Heyvaerts,J., Priest,E.R., and Rust,D.M. 1977, ApJ 216, 123
Hirayama,T. 1994, Solar Phys. 34, 323
Holt,S.S. and Ramaty,R. 1969, Solar Phys. 8, 119
Karpen,J.T., Antiochos,S,K., and DeVore,C.R. 1995, ApJ 450, 422
Karpen,J.T., Antiochos,S.K., DeVore,C.R., and Golub,L. 1998, ApJ 495, 491
Kliem,B. 1994, ApJS 90, 719

Klimchuk,J.A. and Sturrock,P.A. 1992, ApJ 385, 344
Kopp,R.A. and Pneuman,G.W. 1976, Solar Phys. 50, 85
Lin,R.P. 1974, Solar Phys. 16, 189
Longcope,D.W. 1996, Solar Phys. 196, 91
Machado,M.E., Moore,R.L., Hernandez,A.M., Rovira,M.G., Hagyard,M., and Smith,J.B.Jr. 1988, ApJ 326, 425
Mariska,J.T., Emslie,A.G., and Li,P. 1989, ApJ 341, 1067
Masuda,S., Kosugi,T., Hara,H., Tsuneta,S., and Ogawara,Y. 1994, Nature 371, No. 6497, 495
Nishio,M., Yaji,K., Kosugi,T., Nakajima,H., Sakurai,T. 1997, ApJ 489, 976
Nitta,N., Dennis,B.R., and Kiplinger,A.L. 1990, ApJ 353, 313
Pick,M., Raoult,A., Trottet,G., Vilmer,N., Strong,K., and Magalhaes,A. 1994, in Proc. Kofu Symp. on "New Look at the Sun with Emphasis on Advanced Observations of Coronal Dynamics and Flares", eds. S.Enome and T.Hirayama, NRO Rep. No. 360, p.263
Ramaty,R., Schwartz,R.A., Enome,S., and Nakajima,H. 1994, ApJ 436, 941
Sakai,J.I. and DeJager,C. 1996, Space Sci.Rev. 77, 1
Sakai J.I. and Ohsawa Y. 1987, Spa.Sci.Reviews 46, 113
Sakao,T. 1994, PhD. Thesis, University of Tokyo
Smith,D.F. 1977, JGR 82, 704
Shibata,K., Masuda,S., Shimojo,M., Hara,H., Yokoyama,T., Tsuneta,S., Kosugi,T., and Ogawara,Y. 1995, ApJ 451, L83
Somov,B.V., Kosugi,T. and Sakao,T. 1997, ApJ 497, 943
Spicer,D.S. 1981, Solar Phys. 71, 115
Sturrock,P.A. 1966, Nature 5050, 695
Tsuneta,S., Hara,H., Shimizu,T., Acton,L.W., Strong,K.T., Hudson,H.S., and Ogawara,Y. 1992, PASJ 44, L63
Tsuneta,S. 1996, ApJ 456, 840
Tsuneta,S., Masuda,S., Kosugi,T., and Sato,J. 1997, ApJ 478, 787